



A numerical study of sedimentation by dripping instabilities in viscous fluids

G.W. Bergantz^{a, *}, J. Ni^b

^a*Department of Geological Sciences and Volcano Systems Center, Box 351310, University of Washington, Seattle, WA 98195, USA*

^b*Advanced Research Computing Services, Weeg Computer Center, University of Iowa, IA, 52242-1589, USA*

Received 17 April 1997; received in revised form 22 July 1998

Abstract

A common instability in metallurgy and geophysics is the dripping of negatively-buoyant, solid–liquid mixtures. We conducted a numerical study of the finite amplitude evolution of multiphase Rayleigh–Taylor instabilities. For systems with a density-weighted average viscosity of less than 0.2, two time scales of sedimentation were observed. Initially, plumes form and merge, and solids disperse throughout the cavity. Final clarification of the carrier phase by hindered Stoke’s settling then occurs. The ratio of the time to clear the mixture to the time for near-uniform dispersal of the solids can be two or three orders of magnitude. Roof sedimentation in more viscous liquids demonstrates a complex time dependence. The solid volume fraction distribution becomes non-topological with features of both viscous and inertially dominated conditions at a given time step. Cyclic sedimentation occurs as the potential energy associated with the initially unstable layer does not decay in a temporally uniform manner. © 1999 Elsevier Science Ltd. All rights reserved.

Keywords: Sedimentation; Rayleigh–Taylor; Mixing; Viscosity; Entrainment

1. Introduction

Multiphase flow is a central element in the processes of heat and mass transfer in metallurgical and geophysical applications (Beckermann and Viskanta, 1993; Marsh, 1996). The cooling of castings and bodies of molten rock can lead to density instabilities that take the form of multiphase drips that fall from the roof (Marsh, 1988; Morse, 1986; Simakin *et al.*, 1994). The density instabilities are dominated by the creation of solids during cooling, since

* Corresponding author. E-mail: bergantz@u.washington.edu

changes in the melt density are typically small and often result from compositional differences. The dynamic stability of the roof zone has been considered by Smith (1988) and Simakin et al. (1994) for geophysical applications. However, neither study has considered the finite-amplitude evolution of the instability, or the explicit role of multiphase interactions.

Laboratory experiments of buoyant instabilities in the finite amplitude regime can yield complex styles of stirring and entrainment (Andrews and Spalding, 1990; Bradley, 1965; Coulliette and Loper, 1995; Griffiths, 1991; Joseph and Renardy, 1993; Kojima et al., 1984; Linden et al., 1994; Shlien and Thompson, 1975; Snider and Andrews, 1994). For the applications considered here, the roof instabilities are of the Rayleigh–Taylor type. Rayleigh–Taylor instabilities are usually modeled as one of two extremes as a function of the Reynolds number [see reviews by Sharp (1984) and Kull (1991)]. At one extreme, the model assumes inviscid conditions, and the density ratio and the wavelength of the perturbation are important in the description of the flow (Tryggvason, 1988). At the other extreme, the model includes the assumption of creeping flow with a vanishing Reynolds number.

Numerical studies of the Rayleigh–Taylor instability can reveal features of both models (Daly, 1967; Glimm et al., 1990; Linden et al., 1994; Tryggvason and Unverdi, 1990; Youngs, 1984; Youngs, 1989; Youngs, 1991). In a numerical study of turbulent entrainment by a two-fluid Rayleigh–Taylor instability, Youngs (1984) developed a relation between the position of the entrainment front and time:

$$h = \alpha Agt^2 \quad (1)$$

where h is the vertical position of the first computational cell where the horizontally-averaged solid fraction has reached some small value, g is the scalar acceleration of gravity and t is time. A is the Atwood ratio, and α is a constant. The Atwood ratio is the difference between the layer and reservoir densities divided by their sum. For a solid–liquid mixture in contact with a pure liquid it is defined as:

$$A = \frac{\rho_m - \rho_L}{\rho_m + \rho_L}, \quad \rho_m = \varepsilon_L \rho_L + \varepsilon_S \rho_S \quad (2)$$

where ε and ρ refer to the volume fraction and mass-averaged density and the subscript L and S refer to the solid and liquid phase. The similarity of Eq. (1) assumes complete loss of memory of initial conditions, and hence negligible dependence on viscosity, which may be difficult to reach in practice. This may be important in geophysical and industrial applications where viscosity can vary dramatically, as a result of compositional changes and changes in local solid fraction. Eq. (1) implies a global time scale for mixing in a system of height H (Linden et al., 1994):

$$\tau = \frac{t}{\sqrt{\frac{H}{Ag}}}. \quad (3)$$

Youngs' (1984, 1989, 1991) numerical experiments demonstrate many features of turbulent mixing for miscible fluids but does not include the specific two-phase physics to account for the influence of solids. The purpose of this study is to document solid–liquid interactions in the

development of viscous, finite amplitude multiphase drips, and to consider the finite Reynolds number regime prior to the onset of fully-turbulent conditions in a system where the vertical length scale is greater than the layer thickness. Of particular interest was the spatial solid fraction distribution that results from stirring with the carrier phase, the efficiency of multiphase plumes as possible agents of rapid clarification of a solid–liquid system, and the utility of the vanishing Reynolds number Rayleigh–Taylor theory for multiphase geophysical and metallurgical applications. Of additional interest is demonstrating a numerical application of the general multiphase model of Ni and Beckermann (1991).

2. Governing equations and numerical implementation

We conducted numerical simulations of isothermal sedimentation to investigate one process of crystal–liquid segregation. The model formulation and governing equations are an extension of the Eulerian–Eulerian two-phase model for advection–reaction of Ni and Beckermann (1991), which itself is a variation of the multiphase theory developed by Drew (1983), Ishii (1975) and Hassanizadeh and Gray (1979). The volume fraction is treated as a continuous variable. The two phases can share any computational node, but retain their identity. In effect, the phase volume fraction within any node is the existence probability of the phase, and provides a node-averaged measure of the degree of mixing or stirring. The utility of this approach has been demonstrated in a number of other applications (Andrews, 1995; Ilegbusi et al., 1997; Ilegbusi and Spalding, 1989; Youngs, 1984; Youngs, 1989; Youngs, 1991).

The conservation of mass for a phase k can be expressed as

$$\frac{\partial}{\partial t}(\varepsilon_k \rho_k) + \nabla \cdot (\varepsilon_k \rho_k \mathbf{v}_k) = 0 \quad (4)$$

where t , and \mathbf{v} refer to the time and volume-averaged intrinsic velocity vector.

The conservation of momentum for a phase k can be written as

$$\begin{aligned} \frac{\partial}{\partial t}(\varepsilon_k \rho_k \mathbf{v}_k) + \nabla \cdot (\varepsilon_k \rho_k \mathbf{v}_k \mathbf{v}_k) = & -\varepsilon_k \nabla P_k + M_k^d + \varepsilon_k \rho_k \mathbf{g} \\ & + \nabla \cdot \{ \mu_k^* [\nabla(\varepsilon_k \mathbf{v}_k) + [\nabla(\varepsilon_k \mathbf{v}_k)]^t - v_S \nabla \varepsilon_k - \nabla \varepsilon_k v_S] \} \end{aligned} \quad (5)$$

where \mathbf{g} refers to the acceleration due to gravity, and M_k^d refers to the dissipative part of the interfacial momentum transfer. For this study, we considered a two-phase system of liquid and solids where subscript k can be taken as L and S , respectively. We also assumed that the solid and liquid have the same pressure which is appropriate if the speed of sound for each phase is large compared to the calculated velocities (Drew, 1983). The interfacial balance and momentum transfer may be modeled in terms of a drag coefficient

$$M_S^d = -M_L^d = -\frac{3}{4} \frac{\varepsilon_S}{\varepsilon_S} \rho_L C_{d\ell} |v_L - v_S| (v_L - v_S) \quad (6)$$

where d_S is the diameter of the crystals, and $C_{d\varepsilon}$ is the generalized drag coefficient which is valid for all solid fractions and includes the permeability after the solid crystals reach the contiguity limit and become stationary (Argwahl and O'Neill, 1988):

$$C_{d\varepsilon} = \left\{ \frac{200(1 - \varepsilon_L)}{Re} + \frac{7}{5} \right\}, \quad Re = \frac{\rho_L \varepsilon_L |v_L - v_S| d_S}{\mu_L}. \quad (7)$$

Based on the rheology of multiphase flow, the liquid dynamic viscosity is taken as $\mu_L^* = \mu_L$ and the solid dynamic viscosity as

$$\mu_S^* = \frac{[1 - \varepsilon_S/\varepsilon_{sp}]^{-2.5\varepsilon_{sp}} - \varepsilon_L}{\varepsilon_S} \mu_L \quad (8)$$

where ε_{sp} is the critical solid volume fraction, above which the crystals forms a rigid structure. At values of the solid fraction greater than the critical solid fraction, μ_S^* becomes infinitely large, forcing the velocity gradients in the solid phase to vanish. For vanishing solid fractions, Eq. (8) reduces to that from the Einstein dilute theory, $\mu_S^* = 3.5 \mu_L$ (Nunziato, 1983). The value of ε_{sp} usually falls between 0.4 and 0.6; a value of 0.5 is used here.

The boundary conditions for the carrier phase are no-slip at the roof and floor and with slip permitted at the sides. These conditions yield a semi-infinite domain if the horizontal extent of the computational domain is greater than the wavelength of the fastest growing instability.

The governing equations were solved using the finite-volume algorithm of Spalding (1985). Details of the numerical algorithm that combine the continuity equations of the separate phases to generate a single pressure can be found there. This approach has been widely used to model a variety of dynamic, two-phase systems (e.g. Samuelsberg and Hjertager, 1996). The geometry is two-dimensional in Cartesian coordinates. The rate of penetration of the mixing zone into the reservoir is greater for 3-d simulations at early times, and the time scale of kinetic energy dissipation is different, however 2-d models have been found to be sufficient for resolving the overall growth-rate of the mixing zone in prior investigations (Youngs, 1991). The numerical implementation of the source terms for sedimentation were verified by comparison with laboratory experiments such as those by Wilson (1953), Garside and Al-Dibouni (1977) and Barnea and Mizrahi (1973). Good agreement was found between the numerical simulations and the laboratory data for the bulk settling velocity, and the rate of propagation and the sharpness of the clarification (or shock) fronts.

A first-order discretization of the phase volume fraction is used here. This approach is prone to numerical diffusion (Andrews, 1995). To assess the sensitivity of the results to numerical diffusion, we undertook a study of grid refinement and characteristic length scale. In discrete particle volume averaging, the minimum grid size is limited by a multiple of the particle size (Celmins, 1988). The first case, with the lowest viscosity, was solved on a 200×250 node grid which is nearly the limit allowed by volume averaging. This case was also run on a 90×130 node grid which provided sufficient resolution to reproduce the macroscopic features of the flow. This same grid was used for the second case and a 90×200 node grid for the third case.

3. Finite amplitude behavior

3.1. Model description

The model system is shown in Fig. 1. A cavity contains a liquid with a strip at the roof with a uniform mixture of solids and liquid. The roof strip is one-fifteenth the height of the cavity. In all three example calculations, the mixed-phase roof strip had an initial solid volume fraction of 0.2 and an initial density ratio of 1.04 between the roof strip and the underlying fluid. The Atwood ratio has a value of 0.02 for all three examples.

The dynamic viscosity of the carrier phase was increased an order of magnitude in each of the three numerical examples. The density-weighted average kinematic viscosity is a system property and is defined as (Menikoff et al., 1977):

$$\bar{\mu} = \frac{\mu_L + \mu_m}{\rho_L + \rho_m}, \quad \mu_m = \varepsilon_L \mu_L^* + \varepsilon_S \mu_S^* \quad (9)$$

and has a value of 0.002 for the first example, 0.02 for the second example and 0.2 for the third.

3.2. Results

Figures 1–3 are characteristic sub-portions of the computed flow field for three values of the density-weighted kinematic viscosity. In all three example calculations, the instability to begin convection resulted from numerical noise or round-off error during the iterative solution of the linearized form of the governing equations.

A macroscopic, time-dependent Reynolds number can be defined as (Griffiths, 1986; Schlien and Thompson, 1975):

$$Re_m = \frac{v\delta}{\eta} \quad (10)$$

where v is the vertical velocity of a downward moving thermal, δ the diameter of the thermal and η the kinematic viscosity. The macroscopic Reynolds number in the first example had values around 200, but reached a maximum of 526. These results indicate that, for a portion of the simulation, the largest-scale eddies are approaching turbulence. The maximum macroscopic Reynolds number for case 3, the high viscosity case, was 22.

The instabilities formed a temporally and spatially complex pattern of interactions. The distinctive temporal characteristic of the flow is the development of larger fluid structures at the expense of smaller structures as the mixture penetrates the lower fluid layer. The complex interaction of negatively buoyant elements leads to merging of plumes. For example, the distinct thermal that lies in the upper-left-center of Fig. 1(b) (centered at a vertical coordinate of 0.6, horizontal coordinate of 0.25) merges into the stalk of the thermal to the left and loses its identity by a scaled time of 6.84 [Fig. 1(c)].

Tryggvason (1988) and Youngs (1984) reported similar interactions among evolving, finite amplitude instabilities. For both viscous and inviscid fluids with an initial perturbation consisting of waves with random amplitude and phase, complex dipole-like structures formed

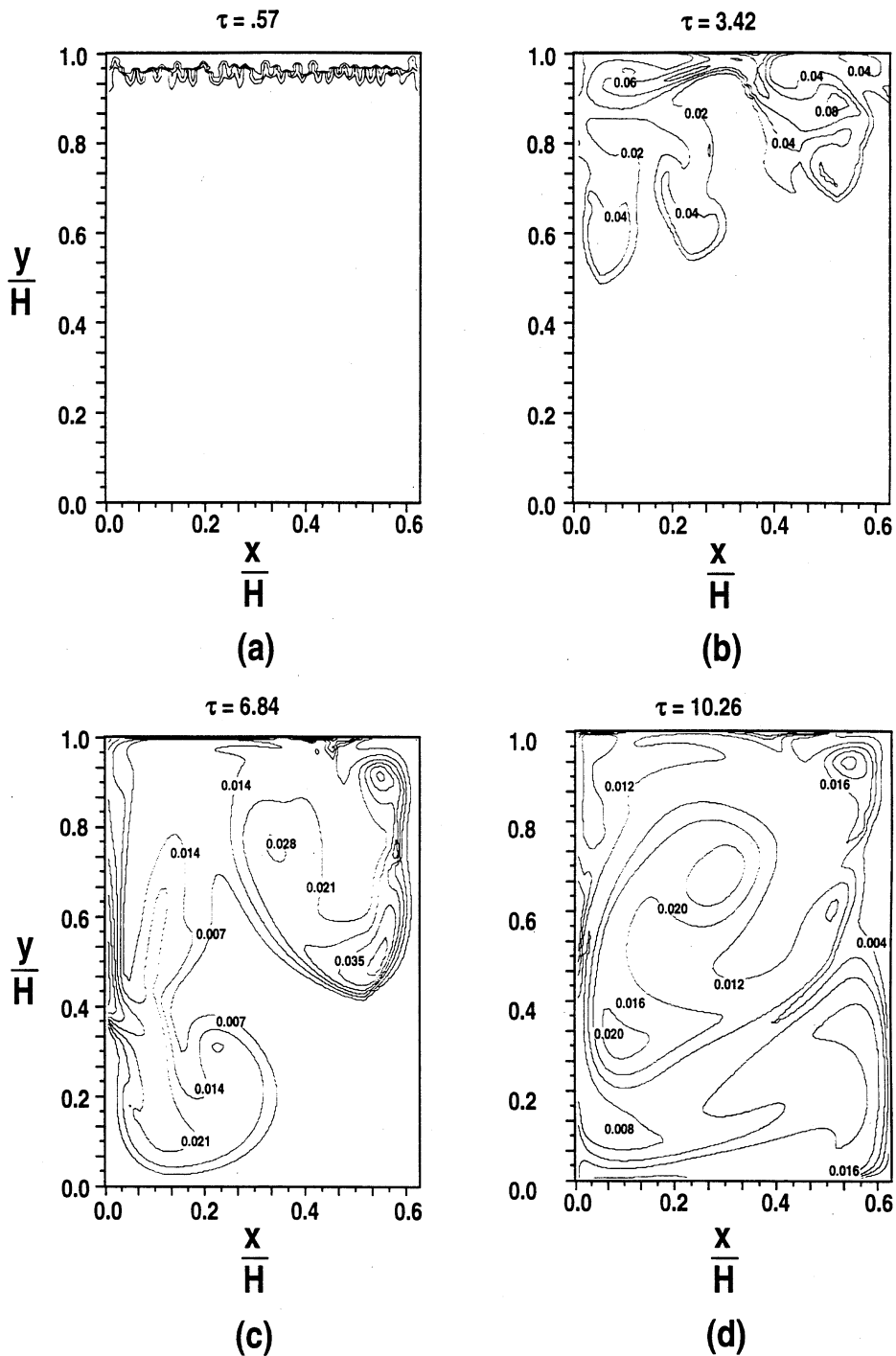


Fig. 1. Case 1, Atwood ratio 0.02, density-weighted average viscosity is 0.002. Contour plot of solid volume fraction at four different scaled times after onset of instability: (a) contour interval 0.05; (b) contour interval 0.02; (c) contour interval 0.007; (d) contour interval 0.04.

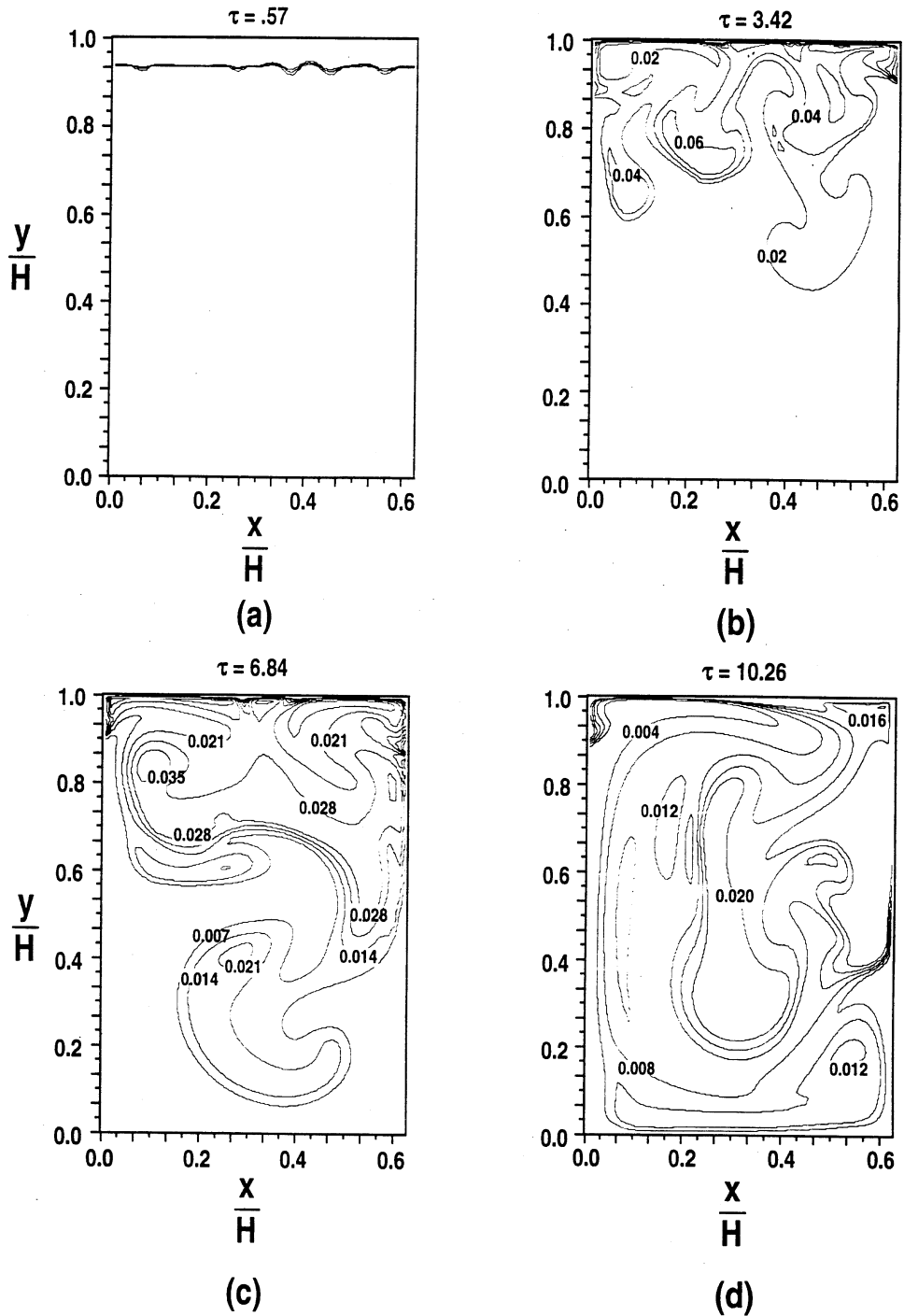


Fig. 2. Case 2, Atwood ratio 0.02, density-weighted average viscosity is 0.02. Contour plot of solid volume fraction at four times after onset of instability: (a) contour interval 0.05; (b) contour interval 0.02; (c) contour interval 0.007; (d) contour interval 0.04.

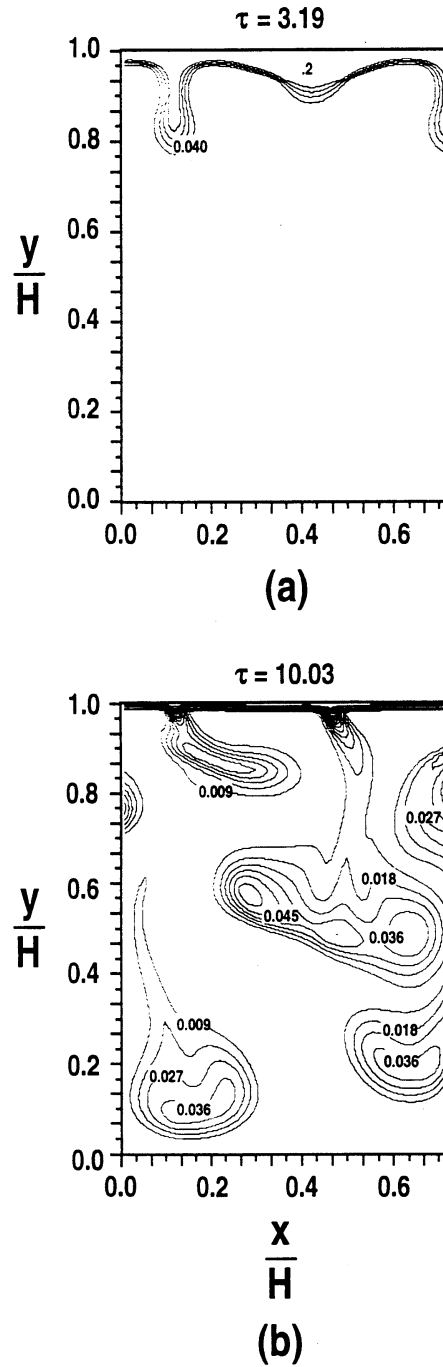


Fig. 3. Case 3, Atwood ratio 0.02, density-weighted average viscosity is 0.2. Contour plot of solid volume fraction at two different times after onset of instability: (a) contour interval 0.04; (b) contour interval 0.009.

that propagated out of the interface mixing zone. The dominant wavelength associated with the instability grew at the expense of smaller instabilities, yielding rather efficient mixing at any vertical position as the entrainment front propagated to the floor. Schmeling (1987) also reported the nonlinear feeding of higher-order terms that overtake the initial wavelength and dominate the final stages for viscous fluids in creeping flow.

The third case, with the most viscous fluid, exhibited transitional behavior. Early in the simulation [Fig. 3(a)] the spacing and amplitude of the instabilities were like those reported by Newhouse and Pozrikidis (1990) for superimposed harmonic perturbations under conditions of creeping flow. The latter stages [Fig. 3(b)] reveal mixed-phase drops that look remarkably like those calculated by Pozrikidis (1990) for the interaction of a prolate drop with a wall under conditions of creeping flow.

In the third case, the entire upper boundary layer did not participate in initial formation of the instabilities. A cyclic process was observed, where only a portion of the upper layer would become unstable, while the remainder held to the upper boundary. The retention of a portion of the dense, mixed-phase layer was due in part to the viscous interaction of the layer with the upper wall, but was dominated by the upward movement of the melt phase. After the initial stage of plume formation and the subsequent diminishment of convective activity, the upper layer issued another set of instabilities, and the process was repeated until the upper layer was nearly exhausted of mixed-phase material. This cyclic sedimentation was not observed in the first two cases. Thus, more viscous liquids will tend to produce an instantaneous non-uniform solid fraction distribution characterized by two populations: a narrow roof layer that is periodically unstable and a region in the lower part of the cavity where plume activity has deposited mixed-phase material.

Fig. 4 is a sedimentation map with contours of horizontally-averaged solid fraction as a function of scaled time for case 1. The contours form a spreading pattern in time that indicates the formation of plumes and thorough dispersal of solids throughout the cavity. There are two distinct time scales of roof sedimentation. The first is the time scale of plume formation, entrainment by stirring of the carrier phase and dispersal of crystals throughout the cavity. The second is the time scale of clarification of the now nearly homogeneous mixture by hindered Stokes settling. The clarification time scale can be obtained from the expression (Ungarish, 1993):

$$t_{Sc} = \frac{H}{V} \left[\frac{1 - \left(\frac{\epsilon_{Sm}}{\epsilon_{Sp}} \right)}{(1 - \epsilon_{Sm})^2} \lambda \right] \quad (11)$$

where H is the height of the cavity, V is the Stoke's velocity, ϵ_{Sm} the mixture solid fraction and λ the dimensionless mixture viscosity:

$$V = \frac{2}{9} \left(\frac{\rho_S - \rho_L}{\rho_L} \right) \frac{a^2 g}{\mu_L}, \quad \lambda = [1 - \epsilon_S / \epsilon_{Sp}]^{-2.5 \epsilon_{Sp}} \quad (12)$$

a is the particle radius, and μ the dynamic viscosity.

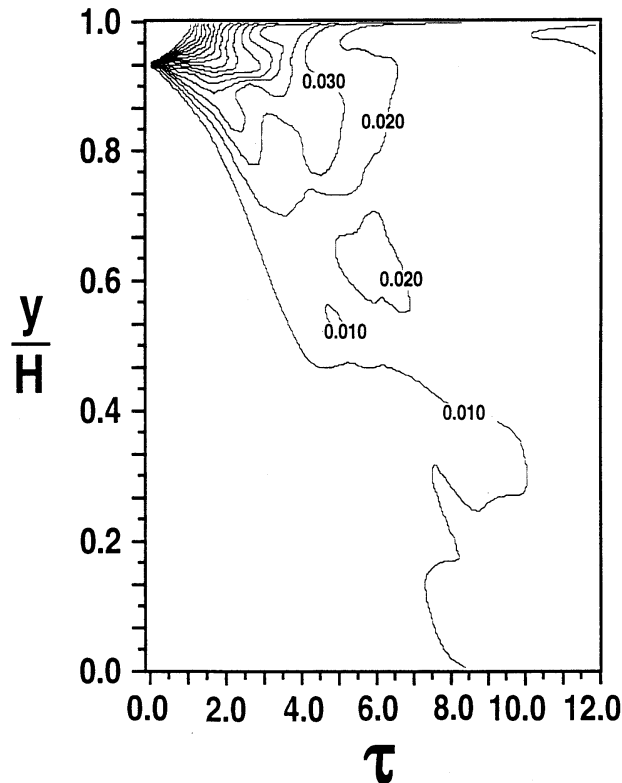


Fig. 4. Sedimentation map for case 1, with contours of horizontally-averaged solid volume fraction as a function of scaled time after onset of instability.

The ratio of the time to clear the mixture to the time to disperse the initial instability is two orders of magnitude for the first case and three orders of magnitude for the second case. The downward movement of the entrainment front for all three cases is given in Fig. 5. The position of the entrainment front is defined as the vertical position of the first computational cell, where the horizontally-averaged solid fraction has reached a value of 0.004. Eq. (1) is shown in Fig. 5, where α was taken to be 0.045, consistent with the experiments of Linden et al. (1994). Eq. (1) gives reasonable agreement for early times; however, once the dense, mixed-phase upper zone has been thoroughly penetrated and disrupted by less dense fluid, Eq. (1) diverges from the results obtained in our calculations. It appears that the time-squared dependence of the position of the entrainment front ceases when the supply of negative buoyancy from the upper layer is exhausted, and the instabilities continue to evolve by mutual interaction and entrainment by stirring of solid-free fluid. The influence of a lower wall is apparent in Fig. 5, where vertical propagation of the entrainment front is slowed while approaching the lower boundary

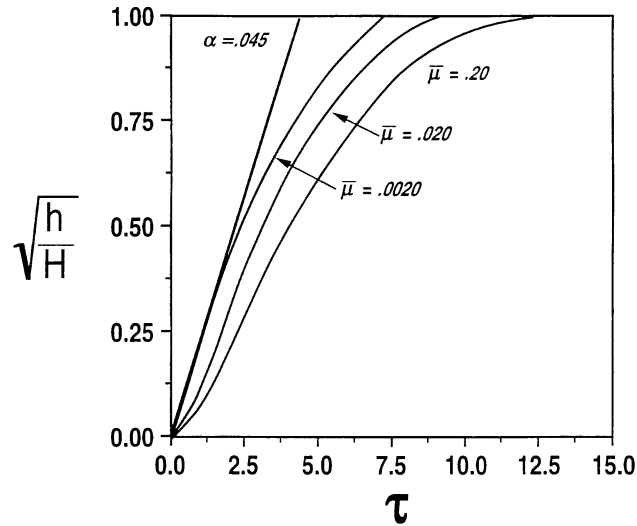


Fig. 5. Position of the entrainment front as a function of time for the three cases considered here. The entrainment front is defined as the vertical position where the solid volume fraction is greater than or equal to 0.004.

4. Discussion

The dimensionless growth rate of the instability as a function of the wave number of a infinitesimal perturbation with zero surface tension can be determined from the relationship given by Newhouse and Pozrikidis (1990):

$$\tilde{\sigma} = \frac{\sigma \mu_L}{\Delta \rho g b} = \frac{1}{2\beta} \left[\frac{\frac{1}{2} \sinh 2\beta - \beta + \frac{1}{\lambda} (\sinh^2 \beta - \beta^2)}{\left(1 - \frac{1}{\lambda}\right) \beta^2 + \left(\cosh \beta + \frac{1}{\lambda} \sinh \beta\right)^2} \right] \tag{11}$$

where σ is the dimensional growth rate, b is the thickness of the unstable layer, and β the dimensionless wave-number, $\beta = 2\pi b/\xi$, where ξ is the wavelength of the perturbation.

For the initial condition of a layer with a 0.2 solid fraction, the fastest-growing wavelength was not observed as a dominant scale of the instabilities in the first two examples until well into the finite amplitude regime, between a scale time of 3–7 (Figs. 2 and 3), and this wavelength did not persist.

The third example, with the highest viscosity, gives better agreement with the predictions of linear theory. However, the spacing of the instabilities that appear in Fig. 3(a) do not have equal amplitudes as a result of the non-harmonic initial perturbation which is likely to be the case in application. The dominant length scale in the finite-amplitude regime is thus difficult to generalize. Some of the initial instabilities retained the initial growth scale and continued to the floor with little mutual interaction. Others merged and coalesced, forming complex shapes with time-dependent characteristic length-scales, much like the first two cases. The process of accumulation of buoyant elements can be seen in Fig. 3(b).

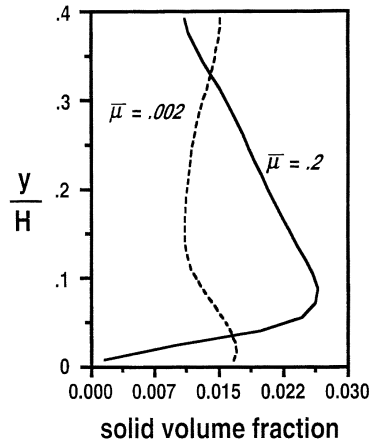


Fig. 6. Horizontally-averaged vertical solid volume fraction distribution for case 1 and case 3 in the lower portion of the system. Case 1 data has a scaled time of 10.25 after onset of instability; case 3 with a scaled time of 27.4 after onset of instability.

The horizontally-averaged solid fraction distribution in the lower portion of the cavity for both the lowest- and highest-viscosity cases is shown in Fig. 6. The solid-fraction distributions represent different model times, but similar points in the respective cycles of dynamic activity. For the low-viscosity case, the curve indicates a nearly uniform, horizontally-averaged, vertical distribution of solids. The more viscous case has approximately 40–50% more solids than the low-viscosity case, as a result of the diminished stirring of the higher viscosity instabilities. Although the higher-viscosity instabilities take more time to traverse the cavity, they arrive at the floor with a higher proportion of solids. The significance is that solid populations on the floor of the cavity with low-viscosity fluid will represent the sedimentation of solids that have been well stirred with their environment. For the higher-viscosity fluids, the instabilities that brought the solids to the floor will have undergone much less entrainment by stirring, and so could retain some memory of conditions at the roof.

5. Conclusions

Numerical experiments of crystal sedimentation in a viscous carrier phase were performed. The results demonstrate at least two time scales in the sedimentation of mixed-phase roof layers: the first is the dispersal time scale, which can be very rapid in low viscosity materials; the second is the time scale for hindered settling of mixture. Previous models of these roof instabilities proposed that the Rayleigh–Taylor conditions might provide a means of rapid transport of the crystals from the roof to the floor without dispersal. For low-viscosity materials, just the opposite occurs: the fluid instabilities provide for substantial mixing.

For the higher-viscosity material simulated in case 3, a cyclic behavior was observed, characterized by the repeated generation of instabilities from a sub-layer of the unstable roof strip. Although the cavity transit time is longer than the times for the lower viscosity cases, the dispersal and consequently dilution by the entrainment of the carrier phase, was less. The solid

fraction distribution typically would have two populations: a spatially restricted, but high solid fraction, region at the roof, and a broader, and a somewhat lower solid fraction distribution at the floor. These results suggest that viscous materials may be more efficient at final clarification of solids that form at the roof, because the difference in transit times between viscous and lower-viscosity materials is not nearly as great as the final clarification of the lower-viscosity, dispersed mixtures.

References

- Andrews, M.J., 1995. Accurate computation of convective transport in transient two-phase flow. *Int. J. Numer. Method. Fluids* 21, 205–222.
- Andrews, M.J., Spalding, D.B., 1990. A simple experiment to investigate two-dimensional mixing by Rayleigh–Taylor instability. *Phys. Fluids A* 2 (6), 922–927.
- Argwahl, P.K., O’Neill, B.K., 1988. Transport phenomena in multi-particle system-1. Pressure drop and friction factors: unifying the hydraulic-radius and submerged object approaches. *Chem. Engng. Sci.* 43 (9), 2487–2499.
- Barnea, E., Mizrahi, J., 1973. A generalized approach to the fluid dynamics of particulate systems, Part 1. General correlation for fluidization and sedimentation in solid multiparticle systems. *Chem. Engng. J.* 5, 171–189.
- Beckermann, C., Viskanta, R., 1993. Mathematical modeling of transport phenomena during alloy solidification. *Appl. Mech. Rev.* 46 (1), 1–27.
- Bradley, W.H., 1965. Vertical density currents. *Science* 150, 1423–1428.
- Celmins, A., 1988. Representation of two-phase flows by volume averaging. *Int. J. Multiphase Flow* 14, 81–90.
- Coulliette, D.L., Loper, D.E., 1995. Experimental, numerical and analytical models of mantle starting plumes. *Phys. Earth Plan. Interior* 92, 143–167.
- Daly, B.J., 1967. Numerical study of two fluid Rayleigh–Taylor instability. *Phys. Fluids* 10 (2), 297–307.
- Drew, D.A., 1983. Mathematical modeling of two-phase flow. *Ann. Rev. of Fluid Mech.* 15, 261–291.
- Garside, J., A-Dibouni, M.R., 1977. Velocity-voidage relationships for fluidization and sedimentation in solid–liquid systems. *Ind. Engng. Chem., Process Des. Dev.* 16 (2), 206–214.
- Glimm, J., Li, X.L., Menikoff, R., Sharp, D.H., Zhang, Q., 1990. A numerical study of bubble interactions in Rayleigh–Taylor instability for compressible fluids. *Phys. Fluids A* 2, 2046–2054.
- Griffiths, R.W., 1986. Thermals in extremely viscous fluids, including the effects of temperature-dependent viscosity. *J. Fluid Mech.* 166, 115–138.
- Griffiths, R.W., 1991. Entrainment and stirring in viscous plumes. *Phys. Fluids A* 3, 1233–1242.
- Hassanzadeh, M., Gray, W.G., 1979. General conservation equations for multi-phase systems: 1. Averaging procedure. *Adv. Water Resour.* 2, 131–144.
- Ilegbusi, O.J., Mat, M., Andrews, M., 1997. The deformation and kinematic mixing of a collapsing interface. *Appl. Math. Model.* 21, 66–76.
- Ilegbusi, O.J., Spalding, D.B., 1989. Prediction of fluid flow and heat transfer characteristics of turbulent shear flows with a two-fluid model of turbulence. *Int. J. Heat Mass Trans.* 32, 767–774.
- Ishii, M., 1975. *Thermo-fluid Dynamic Theory of Two-Phase Flow*. Eyrolles, Paris.
- Joseph, D.D., Renardy, Y.Y., 1993. *Fundamentals of Two-Fluid Dynamics, Part II: Lubricated Transport, Drops and Miscible Liquids*, 445. Springer, Berlin.
- Kojima, M., Hinch, E.J., Acrivos, A., 1984. The formation and expansion of a toroidal drop in a viscous fluid. *Phys. Fluids* 27 (1), 19–32.
- Kull, H., 1991. Theory of the Rayleigh-Taylor instability. *Phys. Rep.* 206, 197–325.
- Linden, P.F., Redondo, J.M., Youngs, D.L., 1994. Molecular mixing in Rayleigh–Taylor instability. *J. Fluid Mech.* 265, 97–124.
- Marsh, B.D., 1988. Crystal capture, sorting and retention in convecting magma. *Geol. Soc. Am. Bull.* 100, 1720–1737.
- Marsh, B.D., 1996. Solidification fronts and magmatic evolution. *Miner. Mag.* 60, 5–40.
- Menikoff, R., Mjolsness, R.C., Sharp, D.H., Zemach, C., 1977. Unstable normal modes for Rayleigh–Taylor instability in viscous fluids. *Phys. Fluids* 20 (12), 2000–2004.
- Morse, S.A., 1986. Thermal structure of crystallizing magma with two-phase convection. *Geol. Mag.* 123 (3), 205–214.
- Newhouse, L.A., Pozrikidas, C., 1990. The Rayleigh-Taylor instability of a viscous liquid layer resting on a plane wall. *J. Fluid Mech.* 217, 615–638.

- Ni, J., Beckermann, C., 1991. A volume-averaged two-phase model for transport phenomena during solidification. *Metall. Trans. B* 22B, 349–361.
- Nunziato, J.W., 1983. A multiphase mixture theory for fluid-particle flows. In: R. E. Meyer (Ed.). *Theory of Dispersed Multiphase Flow*. Academic Press, New York, pp. 191–226.
- Pozrikidis, C., 1990. Deformation of a liquid drop moving normal to a plane wall. *J. Fluid Mech.* 215, 331–363.
- Samuelsberg, A., Hjertager, B.H., 1996. An experimental and numerical study of flow patterns in a circulating fluidized bed reactor. *Int. J. Multiphase Flow* 22 (3), 575–591.
- Schlien, D.J., Thompson, D.W., 1975. Some experiments on the motion of an isolated laminar thermal. *J. Fluid Mech.* 72, 35–47.
- Schmeling, H., 1987. On the relation between initial conditions and late stages of Rayleigh–Taylor instabilities. *Tectonophysics* 133, 65–80.
- Sharp, D.H., 1984. An overview of Rayleigh–Taylor instability. *Physica* 12D, 2–18.
- Simakin, A., Trubitsyn, V., Schmeling, H., 1994. Structure of the upper boundary layer of a solidifying intrusion with crystal sedimentation. *Earth Planet. Sci. Lett.* 126, 333–349.
- Smith, M.K., 1988. Thermal convection during the directional solidification of a pure liquid with variable viscosity. *J. Fluid Mech.* 188, 547–570.
- Snider, D.M., Andrews, M.J., 1994. Rayleigh–Taylor and shear driven mixing with an unstable thermal stratification. *Phys. Fluids* 6, 3324–3334.
- Spalding, D.B., 1985. Computer simulation of two-phase flows with special reference to nuclear reactor systems. In: R.W. Lewis, K. Morgan, J.A. Johnsen, W.R. Smith (Eds.). *Computational Techniques in Heat Transfer*. Pineridge Press, Swansea, pp. 1–44.
- Tryggvason, G., 1988. Numerical simulations of the Rayleigh–Taylor instability. *J. Computat. Phys.* 75, 253–282.
- Tryggvason, G., Unverdi, S.O., 1990. Computations of three-dimensional Rayleigh–Taylor instability. *Phys. Fluids A2*, 656–659.
- Ungarish, M. 1993. *Hydrodynamics of Suspensions*. 317. Springer, New York.
- Wilson, B.W., 1953. The sedimentation of dense suspensions of microscopic spheres. *Aust. J. Appl. Sci.* , 274–299.
- Youngs, D.L., 1984. Numerical simulation of turbulent mixing by Rayleigh–Taylor instability. *Physica* 12D, 32–44.
- Youngs, D.L., 1989. Modelling turbulent mixing by Rayleigh–Taylor instability. *Physica* 37D, 270–287.
- Youngs, D.L., 1991. Three-dimensional numerical simulation of turbulent mixing by Rayleigh–Taylor instability. *Phys. Fluids A* 3 (5), 1312–1320.